

# AMERICAN METEOROLOGICAL SOCIETY

*Journal of Climate*

## EARLY ONLINE RELEASE

This is a preliminary PDF of the author-produced manuscript that has been peer-reviewed and accepted for publication. Since it is being posted so soon after acceptance, it has not yet been copyedited, formatted, or processed by AMS Publications. This preliminary version of the manuscript may be downloaded, distributed, and cited, but please be aware that there will be visual differences and possibly some content differences between this version and the final published version.

The DOI for this manuscript is doi: 10.1175/JCLI-D-16-0581.1

The final published version of this manuscript will replace the preliminary version at the above DOI once it is available.

If you would like to cite this EOR in a separate work, please use the following full citation:

He, J., M. Winton, G. Vecchi, L. Jia, and M. Rugenstein, 2016: Transient Climate Sensitivity Depends on Base Climate Ocean Circulation. *J. Climate*. doi:10.1175/JCLI-D-16-0581.1, in press.

© 2016 American Meteorological Society



1

## 2 Transient Climate Sensitivity Depends on Base Climate Ocean Circulation

3

4

5 Jie He<sup>1</sup>, Michael Winton<sup>2</sup>, Gabriel Vecchi<sup>2</sup>, Liwei Jia<sup>1</sup> & Maria Rugenstein<sup>3</sup>

6

7

8 1. Princeton University, and NOAA/Geophysical Fluid Dynamics Laboratory, Princeton,  
9 New Jersey

10 2. NOAA/Geophysical Fluid Dynamics Laboratory, Princeton, New Jersey

11 3. Institute for Atmospheric and Climate Science, ETH Zürich, Zürich, Switzerland

12

13

14

15

16

To be submitted to *J. Climate*

17

18 Corresponding author's address:

19 Jie He

20 Geophysical Fluid Dynamics Laboratory

21 Princeton University

22 201 Forrestal Road, Princeton, NJ, 08540, USA

23 E-mail: [Jie.He@noaa.gov](mailto:Jie.He@noaa.gov)

24      **Abstract**

25            There is large uncertainty in the simulation of transient climate sensitivity. This  
26       study aims to understand how such uncertainty is related to the simulation of the base  
27       climate by comparing two simulations with the same model but in which CO<sub>2</sub> is  
28       increased from either a pre-industrial (1860) or a present-day (1990) control simulation.  
29       This allows different base climate ocean circulations that are representative of those in  
30       current climate models to be imposed upon a single model. As a result, the model  
31       projects different transient climate sensitivities that are comparable to the multi-model  
32       spread. The greater warming in the 1990-start run occurs primarily at high-latitudes and  
33       particularly over regions of oceanic convection. In the 1990-start run, ocean overturning  
34       circulations are initially weaker and weaken less from CO<sub>2</sub> forcing. In consequence, there  
35       are smaller reductions in the poleward ocean heat transport, leading to less tropical ocean  
36       heat storage and less moderated high-latitude surface warming. This process is evident in  
37       both hemispheres, with changes in the Atlantic meridional overturning circulation and the  
38       Antarctic bottom water formation dominating the warming differences in each  
39       hemisphere. The high-latitude warming in the 1990-start run is enhanced through albedo  
40       and cloud feedbacks, resulting in a smaller ocean heat uptake efficacy. The results  
41       highlight the importance of improving the base climate ocean circulation in order to  
42       provide a reasonable starting point for assessments of past climate change and the  
43       projection of future climate change.

44

45        **1. Introduction**

46            Climate models project a large range of surface warming from greenhouse gas  
47            forcing. As documented in the Intergovernmental Panel on Climate Change Fifth  
48            Assessment Report (Stocker et al. 2013), the transient climate response (TCR), defined as  
49            the global mean surface temperature increase at year 70 of a 1pctCO<sub>2</sub> experiment., varies  
50            by more than a factor of two. The large inter-model spread in transient warming emanates  
51            from not only the uncertainty in radiative forcing and atmospheric feedbacks (e.g.,  
52            Hansen et al. 1984; Raper et al. 2002) but also the uncertainty in the rate of heat uptake  
53            by the ocean (Meehl et al. 2005; Stouffer et al. 2006b; Boé et al. 2009) and the efficacy  
54            of that heat uptake (Winton et al. 2010; Geoffroy et al. 2013).

55            A considerable amount of heat taken up by the ocean resides in the deep ocean  
56            (Gregory 2000; Raper et al. 2002; Kostov et al. 2014; Exarchou et al. 2014; Rugenstein et  
57            al. 2016b), which is continuously filled by polar sinking water masses through the  
58            overturning circulation. As a result, the formation of deep water plays an important role  
59            in setting the ocean heat content and heat transport. In addition, during the transformation  
60            of surface water into dense sinking water, heat is released into the atmosphere, warming  
61            the surface climate in the high latitudes (e.g., Winton 2003; Frierson et al. 2013).  
62            Changes in circulation, including the convection, are an important factor in the projection  
63            of transient warming (Rugenstein et al. 2013; Winton et al. 2014).

64            In the Northern Hemisphere, the sinking water is primarily formed in the  
65            Labrador and Nordic seas and flows southward as part of the Atlantic meridional  
66            overturning circulation (AMOC). Models have shown that AMOC is important in  
67            regulating the pace of surface warming. The representation of AMOC varies greatly

68 among models, contributing substantially to the uncertainty in transient warming (e.g.,  
69 Gregory et al. 2005; Solomon 2007; Medhaug and Furevik 2011). Particularly, it has  
70 been shown that models with a stronger AMOC (Kostov et al. 2014) and a greater  
71 AMOC decline (Xie and Vallis 2012; Rugenstein et al. 2013; Winton et al. 2013, 2014)  
72 tend to project a slower transient warming.

73 In the Southern Hemisphere, convection primarily occurs in the Weddell Sea, the  
74 Ross Sea and the Adelie Coast to produce the Antarctic bottom water (AABW, Orsi et al.  
75 1999), which fills the wide abyssal ocean. Observations between the 1980s and 2000s  
76 indicate a reduction of the AABW production and an associated warming of AABW,  
77 which accounts for most of the ocean heat uptake below 2000m (Purkey and Johnson  
78 2010, 2012, 2013). Unfortunately, this process cannot be accurately represented by  
79 climate models due to their large biases in Southern Ocean circulation (e.g., Russell et al.  
80 2006; Downes et al. 2015). For example, the second phase of the Coordinated Ocean-ice  
81 Reference Experiments shows large spread in AABW formation from state-of-the-art  
82 climate models, ranging from 20Sv to nonexistent (Farneti et al. 2015). The surface  
83 climatic impact of Southern Hemisphere convection is far less studied compared to its  
84 Northern Hemisphere counterpart; and the extent to which the simulation of AABW  
85 formation influences the global transient warming is yet to be determined.

86 To examine the impact of high-latitude convection on transient climate  
87 sensitivity, we compare two global warming experiments with the same model but  
88 initialized from different control runs: the one that starts from the pre-industrial control  
89 run has a stronger initial AMOC and AABW production than the one that starts from the  
90 present-day control run. Compared to the traditional approach of multi-model

91 comparison, our approach is more effective at narrowing down the uncertainty to the  
92 simulation of the base climate as the responses in both experiments are governed by the  
93 same formula. This procedure can be used to determine the specific physical processes  
94 that need to be constrained for accurately projecting transient climate sensitivity.

95 For a more pragmatic purpose, this study also aims to examine whether the  
96 climate sensitivity observed or simulated from a low greenhouse gas condition can be  
97 directly applied to the contemporary climate change. For example, the pre-industrial  
98 condition has been commonly used as the starting point for projecting TCR (e.g., Taylor  
99 et al. 2012). This is a convenient choice since the pre-industrial climate can be assumed  
100 as an equilibrium state. However, because the base climate has changed substantially  
101 since the pre-industrial era, it is unclear to what extent the pre-industrial based TCR can  
102 be used to inform about future warming. Our study will help understand this matter by  
103 comparing the TCR simulated from pre-industrial and present-day base climates.

104

## 105 **2. Model Simulation**

106 The experiments used in this study are conducted with the GFDL forecast-  
107 oriented low ocean resolution model (FLOR). FLOR is built from the high-resolution  
108 Coupled Model version 2.5 (CM2.5; Delworth et al. 2012) by retaining its atmosphere  
109 and land resolution (approximately 50km) and reducing its ocean and sea ice resolution  
110 from approximately  $1/4^\circ$  to approximately  $1^\circ$ . The combination of high-resolution  
111 atmosphere and relatively low-resolution ocean was originally designed for enhancing  
112 regional climate forecasting while maintaining a reasonable computational cost, as

113 detailed by Vecchi et al. (2014). The version of the FLOR model used in this experiment  
114 is the one labeled FLOR-B01 in Vecchi et al. (2014) and Winton et al. (2014).

115 We conduct a pre-industrial control run with 1860 atmospheric composition and a  
116 present-day control run with 1990 atmospheric composition. Both control runs are  
117 initialized with 1990 ocean and atmosphere observations that are assimilated into FLOR  
118 simulations (Zhang et al. 2007). Using such initialization is merely out of convenience  
119 since we do not have a spun-up FLOR. We do not wish the model to mimic the  
120 observations; instead, we hope to obtain the model's climates under the 1860 and 1990  
121 forcings for the respective perturbation runs. This normally requires a long spin-up from  
122 each control run. As shown in Supplementary Figure S1, both control runs experience  
123 drastic adjustments in the first few decades and remain relatively stable after 100 years.  
124 We perform two realizations of 1pctCO<sub>2</sub> simulations branching off each control run after  
125 year 100. In the 1pctCO<sub>2</sub> simulations, CO<sub>2</sub> increases by 1% per year for 70 years till  
126 doubling and is held fixed afterwards for another 170 years.

127 With the 100-year spin-up, models still experience climate drift during the  
128 1pctCO<sub>2</sub> simulations: both the 1860 and 1990 control runs have a global mean surface  
129 warming of about 0.15K per 100 years. This remains a caveat in the interpretation of our  
130 results. To minimize the impact of climate drift, we report all perturbation quantities as  
131 the difference between the corresponding years of the perturbed and control runs.  
132 Although the lack of sufficient spin-up is not ideal, our goal is to study the impact of  
133 differences in the base climate ocean circulation, which are essentially not affected by the  
134 climate drift (Supplementary Material). We also conduct 1pctCO<sub>2</sub> simulations with an  
135 additional 400-year spin-up, which yields consistent results (Supplementary Material).

136

137   **3. Results**

138    a. Overview of transient warming

139       The 1990-start run warms substantially more than the 1860-start run for the  
140       duration of the 1pctCO<sub>2</sub> simulations (Fig. 1). The warming difference is seen in both  
141       ensemble members and develops primarily during the CO<sub>2</sub> increasing period. The  
142       increase in global mean surface temperature averaged over the last 50 years of the  
143       simulation (years 191-240) is 27% larger in the 1990-start run. The difference in TCR  
144       (estimated as the warming averaged over year 61-80) is 0.25K, which is comparable to  
145       the CMIP5 multi-model standard deviation of 0.35K (Gregory et al. 2015). Therefore, in  
146       this model, the projection of transient surface warming depends strongly on its starting  
147       point.

148       Figure 2 shows the spatial pattern of surface temperature changes. A polar  
149       amplification can be found in both simulations and is substantially stronger in the 1990-  
150       start run. In addition, there are large concentrated warming differences in high-latitude  
151       convective regions. In the 1860-start run, convective regions, particularly in the north  
152       Atlantic and the Weddell Sea, become colder (Fig. 2b), which is likely associated with a  
153       weakening of convection and a reduction in upward surface heat flux (Weaver et al.  
154       2007; Newsom et al. 2016; Trossman et al. 2016). In the 1990-start run, the cooling is  
155       much weaker in the north Atlantic and absent in the Weddell Sea. These concentrated  
156       warming differences indicate an important connection to changes in high-latitude  
157       convection and overturning circulation, which will be examined in more detail later.

158 On global scale, the transient surface warming can be thought of as being  
159 determined by three parameters: the equilibrium climate sensitivity (ECS), the ocean heat  
160 uptake efficiency and the ocean heat uptake efficacy (Winton et al. 2010):

161 
$$\partial T = ECS \cdot \frac{R}{R + ECS \cdot \varepsilon \cdot \gamma} \quad (1)$$

162 where  $\partial T$  is the transient surface warming,  $R$  is the radiative forcing of doubled CO<sub>2</sub>  
163 (estimated as 3.5W/m<sup>2</sup> for both simulations from radiation code),  $\varepsilon$  is the ocean heat  
164 uptake efficacy,  $\gamma$  is the ocean heat uptake efficiency.

165 The ocean heat uptake efficiency is defined as

166 
$$\gamma = N / \partial T \quad (2)$$

167 where  $N$  is the net heat uptake, which is dominated by the ocean. The ocean heat uptake  
168 efficiency largely reflects the effectiveness of the deep ocean in absorbing the excess heat  
169 from radiative forcing, and a large efficiency acts to slow down surface warming  
170 (Gregory and Mitchell 1997; Raper et al. 2002).

171 The ocean heat uptake efficacy is defined as the global surface temperature  
172 impact of heat uptake relative to the impact of CO<sub>2</sub> radiative forcing (Winton et al. 2010):

173 
$$\varepsilon = \frac{R / ECS}{N / (ECS - \partial T)} \quad (3)$$

174 It is essentially the ratio between the equilibrium radiative feedback and feedback of the  
175 ocean heat uptake. The efficacy reflects how ocean heat uptake affects the surface  
176 temperature through surface heat flux pattern induced feedback response, and a large  
177 efficacy acts to slow down surface warming (e.g., Rugenstein et al. 2016a).

178 The ECS, the ocean heat uptake efficiency and efficacy are visualized in Figure 3.  
179 A linear extrapolation of the surface temperature - top of atmosphere (TOA) radiation

180 relationship following Gregory et al. (2004) indicates roughly equal ECS (3.27K for  
181 1860-start and 3.30K for 1990-start) and equilibrium radiative feedbacks from the 1990-  
182 start and 1860-start runs.

183 The average ocean heat uptake efficiency for the CO<sub>2</sub> stabilizing period is shown  
184 as the slope of the dashed line in Figure 3, which connects the point of average surface  
185 temperature change and average TOA radiation change with the (0, 0) point. The  
186 efficiency is lower in the 1990-start run throughout the simulation and 28% lower during  
187 the CO<sub>2</sub> stabilization period. The heat uptake efficacy for the CO<sub>2</sub> stabilizing period is  
188 show as the ratio of the CO<sub>2</sub> radiative forcing (3.5W/m<sup>2</sup>) to the y-intercept of the solid  
189 lines in Figure 3. The efficacy is 1.47 for the 1990-start run and 2.01 for the 1860-start  
190 run. Therefore, both the smaller heat uptake efficiency and the smaller efficacy in the  
191 1990-start run account for its larger transient warming.

192

193 b. Ocean heat uptake and heat transport

194 The ocean heat uptake pattern is shown in Figure 4. In the Northern Hemisphere,  
195 heat uptake primarily occurs in the north Atlantic convective regions (Figs. 4a and 4b)  
196 and is overall smaller in the 1990-start run (Fig. 4c). In the Southern Hemisphere, heat  
197 uptake is spread over most of the Southern Ocean. The most noticeable difference  
198 between the two runs is in the Weddell Sea, where only the 1860-start run shows positive  
199 heat uptake. Some quantitative differences can also be found throughout the Southern  
200 Ocean, with somewhat complex structures. Since high-latitude convection is often  
201 associated with heat being released into the atmosphere, the smaller heat uptake at  
202 convective regions in the 1990-start run indicates a smaller weakening of convection.

203       Figure 5 shows the climatology and changes of mixed-layer depth, which is  
204       defined as the depth where the buoyancy difference with respect to the surface level is  
205       greater than or equal to  $0.0003 \text{ m/s}^2$  and can be used as a measure of convection (Stouffer  
206       et al. 2006a). As shown in the right column of Figure 5, both the 1990-start and 1860-  
207       start runs project a general reduction in mixed-layer depth, particularly at convective  
208       regions, indicating a weakening of convection. Consistent with the differences in heat  
209       uptake (Fig. 4c), the 1990-start run shows a smaller weakening of convection in the north  
210       Atlantic and the Weddell Sea (Fig 5, right column). The smaller weakening is associated  
211       with the weaker initial convection, as the difference in the change (Fig. 5f) is almost  
212       exactly the opposite of the control climatology (Fig. 5c). This is consistent with previous  
213       studies (Gregory et al. 2005; Weaver et al. 2007; Newsom et al. 2016), which found that  
214       the weakening of convection largely depends on its initial strength.

215       To complement the high-latitude mixed-layer depth, we present the zonally  
216       integrated meridional overturning circulation (MOC) in Figure 6. The climatological  
217       MOC consists of an upper cell dominated by the AMOC and a lower cell dominated by  
218       the AABW formation (Figs. 6a and 6b). As shown in Figure 6c, the 1990 control run has  
219       a weaker and shallower AMOC. Although the 1990 control run shows a stronger  
220       upwelling poleward of  $50^\circ\text{S}$ , it has a weaker lower cell as a result of its weaker  
221       convection in the Weddell Sea (Fig. 5c). In addition, the two control runs have little  
222       difference in the Antarctic Circumpolar Current transport (only 1.7% stronger in the 1990  
223       control run), likely due to the cancellation between wind forcing and eddy adjustment  
224       (Meredith et al. 2012; Morrison and Hogg 2013). In the 1pctCO<sub>2</sub> simulations, both the

225 AMOC and the AABW formation weaken. The weakening is smaller in the 1990-start  
226 run (Fig. 6f), which is again consistent with its weaker initial circulation (Fig. 6c).

227 To understand the connection between the circulation changes and transient  
228 sensitivity, we compare hemispheric surface warming, MOC weakening and changes in  
229 poleward heat transport for the two 1pctCO<sub>2</sub> simulations (Fig. 7). The AMOC index is  
230 defined as the maximum stream function at 40°N, whereas the AABW index is defined as  
231 the minimum stream function multiplied by -1 at 69°S. These latitudes are chosen  
232 because they exhibit the strongest AMOC and AABW formation, respectively in FLOR's  
233 pre-industrial control run; using a wider range of latitudes for the definition of the indices  
234 would yield similar results (not shown). Changes in the global poleward heat transport  
235 are calculated at 40° latitude. We treat this latitude as the lower bound of high-latitude  
236 regions mainly because AMOC is the strongest at 40°N, but our results are not very  
237 sensitive to this choice. Because sub-grid scale heat transport was not saved, we calculate  
238 poleward heat transport as the residual between ocean heat content tendency and changes  
239 in surface heat flux averaged poleward of 40°. We note that this is not an exact  
240 calculation because we did not account for the varying thickness of the top and bottom  
241 grid cells when obtaining the ocean heat storage. We will further discuss this caveat in  
242 Section 3c.

243 As shown in Figures 7a and 7d, the Northern and Southern Hemispheres  
244 (primarily at high-latitudes, Fig. 2c) contribute about equally to the global difference in  
245 transient warming. For the Northern Hemisphere, the AMOC weakens initially and  
246 stabilizes around year 100 when the CO<sub>2</sub> concentration is stabilized (Fig. 7b). The  
247 AMOC in the 1860-start run is initially 4Sv stronger and eventually reaches similar

248 amplitude as that in the 1990-start run, which means a greater weakening in the 1860-  
249 start run. As a result, it has a larger reduction in the poleward ocean heat transport (Fig.  
250 7c), leading to a more moderated northern high-latitude warming (Figs. 7a and 2c). In  
251 addition, the temporal variability of Northern Hemisphere warming and heat transport  
252 change is generally consistent with the variability of AMOC change (black lines in Fig.  
253 7). For example, during the first 35 years, the 1860-start run undergoes a faster AMOC  
254 weakening; correspondingly, it shows a faster reduction in poleward ocean heat transport  
255 and a slower warming. During years 130 to 160, the AMOC recovers in the 1860-start  
256 run leading to a recovery in poleward heat transport and an accelerated Northern  
257 Hemisphere warming, which does not occur in the 1990-start run. These results are  
258 consistent with Rugenstein et al. (2013), who found a similar relationship between  
259 AMOC weakening and high-latitude warming in two pairs of closely related GFDL  
260 models.

261 In the Southern Hemisphere, the warming difference shows a steady development  
262 during the first 140 years (Fig. 7d), similar to the difference in AABW decline (7e). After  
263 year 140, the AABW formation stabilizes at similar amplitudes and the separation in  
264 surface warming slows down. This relationship is consistent with the fact that much of  
265 the Southern Hemisphere warming difference is concentrated over the Weddell Sea (Fig.  
266 2c), where the 1860-start run shows a reduction in upward surface heat flux (Fig. 4b) and  
267 a surface cooling (Fig. 2b).

268 The cause and effect in the concurrence of AABW weakening and reduced  
269 surface heat loss are yet to be determined and it is likely that they assist in each other's  
270 development. I.e., the reduced surface heat loss could weaken convection through

271 buoyancy forcing (Newsom et al. 2016), whereas the weakening of the overturning  
272 circulation could also reduce the upward heat release by decreasing poleward ocean heat  
273 transport, similar to the process in the northern high-latitude (e.g., Winton et al. 2013;  
274 Rugenstein et al. 2013). Indeed, the Southern Hemisphere poleward heat transport shows  
275 a greater reduction in the 1860-start run. This is consistent with its greater weakening of  
276 the lower cell, which is the dominant difference in Southern Hemisphere MOC (Fig. 6f).  
277 Differences in the upper cell, albeit smaller, may also be important, considering the much  
278 larger temperature gradient in the upper ocean. Further studies are needed to understand  
279 these processes.

280

281 c. Global ocean heat budget

282 To summarize the relationship between ocean heat transport and transient  
283 warming, we present the ocean heat budget for the northern and southern high-latitudes  
284 and the tropics (Fig. 8). The three regions are bounded by the 40° latitude. For each  
285 region, we calculate changes in surface heat flux and ocean heat storage tendency directly  
286 from the model output, and estimate changes in ocean heat transport as the difference  
287 between the two. Because we did not account for the varying thickness of the top and  
288 bottom grid cells when calculating the ocean heat storage, there is a small difference (less  
289 than 2%) between the global surface heat flux change and ocean heat storage tendency.  
290 As indicated by the colored arrows, the ocean circulation transports heat poleward from  
291 the tropics and eventually releases it into the atmosphere in the high-latitude. As the  
292 circulation weakens, the poleward heat transport is reduced and less heat is released into  
293 the high-latitude atmosphere, thereby moderating high-latitude warming.

294 In the 1860-start run, the circulation is initially stronger and weakens more,  
295 leading to a larger reduction in poleward heat transport and a slower high-latitude  
296 warming. Correspondingly, there is more heat uptake in high-latitudes. Most of the high-  
297 latitude heat uptake is stored in the tropics through the reduced poleward heat transport.  
298 The large high-latitude heat uptake relative to the tropics in the 1860-start run is also  
299 consistent with its large heat uptake efficacy, as studies have shown that the cooling  
300 impact of heat uptake is more effective in the high-latitude than the tropics (Kang and  
301 Xie 2014; Rose et al. 2014).

302

303 d. Heat uptake efficacy and transient feedback

304 The greater high-latitude warming of the 1990-start run induced by its smaller  
305 reduction in poleward heat transport can be further amplified by atmospheric radiative  
306 feedbacks, as indicated by its smaller ocean heat uptake efficacy (Fig. 3). To determine  
307 the source of the efficacy difference, we calculate the transient radiative feedbacks for the  
308 CO<sub>2</sub> stabilization period using the GFDL model radiative kernels (Soden et al. 2008).

309 As shown in Table 1, the kernel based transient radiative feedback is 0.15  
310 W/m<sup>2</sup>/K higher in the 1990-start run. This is an underestimation compared to those  
311 directly calculated using the average TOA radiation and surface temperature change,  
312 which yields a 0.29 W/m<sup>2</sup>/K higher feedback in the 1990-start run. The disparity is likely  
313 caused by the uncertainty in the cloud radiative kernels, but the uncertainty in other  
314 radiative kernels and the CO<sub>2</sub> radiative forcing may also contribute. Here, we assume the  
315 accuracy of the kernel based temperature, water vapor and albedo feedbacks and show  
316 the corrected cloud feedback and total feedback in the parentheses.

317       The higher transient feedback in the 1990-start run is partly associated with the  
318       higher albedo feedback and mainly with the greater cloud feedback. This is consistent  
319       with previous studies (Winton 2003; Rose et al. 2014; Trossman et al. 2016; Zhang et al.  
320       2010), which showed that cloud feedback is the dominant radiative feedback mechanism  
321       that responds to ocean circulation change. The larger cloud feedback in the 1990-start run  
322       is primarily associated with its greater reduction in high-latitude low cloud (figures not  
323       shown). The greater low cloud reduction is possibly caused by the larger decrease in  
324       high-latitude tropospheric stability (Winton 2003) associated with the higher polar  
325       amplification (Fig. 2).

326

#### 327       **4. Conclusions and discussion**

328       In this study, we compared the transient warming in the 1pctCO<sub>2</sub> simulations  
329       initialized from an 1860 control run and a 1990 control run. Previous studies showed that  
330       TCR could be sensitive to the differences in initial conditions that result from internal  
331       variability and model drift (Gupta et al. 2012; Liang et al. 2013a,b). The main objective  
332       of this study is to understand the specific model biases in the simulation of base climate  
333       ocean circulation that potentially degrade the projection of transient climate sensitivity.

334       The global mean surface temperature increases substantially faster in the 1990-  
335       start run compared to the 1860-start run. The greater transient warming is attributed to the  
336       smaller ocean heat uptake efficiency and smaller ocean heat uptake efficacy. In the 1990-  
337       start run, the overturning circulations are initially weaker and thereby weaken less from  
338       CO<sub>2</sub> forcing. As a result, there is a smaller reduction in poleward heat transport leading to

339 a faster high-latitude warming. The warming disparity is further amplified partially  
340 through albedo feedback and primarily through cloud feedback.

341 The initial circulation difference in the two simulations is dominated by their  
342 differences in the AMOC and the AABW formation. The stronger initial AMOC and  
343 AABW formation in the 1860-start run allows a larger weakening, which leads to a  
344 surface cooling in the convective regions and a moderated high-latitude warming in the  
345 corresponding hemispheres. This cooling effect of ocean circulation is much less  
346 appreciable in the 1990-start run since the circulation is already substantially weakened at  
347 the beginning of the simulation. One may think of the slower transient warming in the  
348 1860-start run as being delayed by the weakening of circulation. However, such “delay”  
349 becomes less effective as the climate continues to warm.

350 Since most climate models project a weakening of the overturning circulation,  
351 their TCRs, which are often simulated from a pre-industrial starting point, are affected by  
352 the “delay” and should be smaller than future warming under the same radiative forcing.  
353 Other factors such as ocean thermal stratification and the increase in radiative feedbacks  
354 may also contribute to the “delay” (e.g., Gregory et al. 2015). Although we have used the  
355 1860 and 1990 control runs to illustrate the importance of the starting point, the ideal  
356 initialization for projecting future TCR should be taken from the present-day simulation,  
357 in which warming is already under way, instead of a control run, which would induce a  
358 cold start retardation (Hasselmann et al. 1993).

359 Although the initial circulation differences in our simulations were artificially  
360 created by modifying the radiative forcing, they are well within the inter-model spread  
361 (Gregory et al. 2005; Farneti et al. 2015). These circulation differences, even imposed

362 upon the same model, would result in differences in TCR that are comparable to the inter-  
363 model spread. This suggests that biases in the base climate ocean circulation, particularly  
364 AMOC and AABW, need to be constrained for accurate projections of transient warming.  
365 The importance of AMOC has been widely addressed (e.g., Meehl et al. 2005;  
366 Rugenstein et al. 2013; Kostov et al. 2014). In comparison, the climatic impact of AABW  
367 formation has received far less attention, partially due to the fact that it is too weak or  
368 even nonexistent in many models (Frölicher et al. 2014; Farneti et al. 2015; Rugenstein et  
369 al. 2016b). In addition, the lack of observation on the strength of Antarctic convection  
370 makes model improvement rather difficult. However, the Weddell polynya of the 1970's  
371 gave evidence of deep convection in the historical period. de Lavergne et al. (2014) found  
372 that almost 1/3 of the CMIP5 climate models do not have such convection in their pre-  
373 industrial simulations. Our results suggest that this might result in an overestimation of  
374 Southern Ocean warming in these models. A recent study (Newsom et al. 2016) showed  
375 that the AABW formation is substantially stronger when the resolution of ocean model  
376 increases from  $1^{\circ}$  to  $0.1^{\circ}$ . Such studies are encouraged for better understanding the  
377 uncertainty in the simulation of AABW.

378

379

380 *Acknowledgements:* We thank Jonathan Gregory and Isaac Held for useful discussions  
381 and Thomas Delworth for the internal review at Geophysical Fluid Dynamics Laboratory.  
382 Thanks also go to Brian Soden and Eui-Seok Chung for providing radiative kernels. Jie  
383 He is supported by the Visiting Scientist Program at the department of Atmospheric and  
384 Oceanic Science, Princeton University.

385    **References**

- 386    Boé, J., A. Hall, and X. Qu, 2009: Deep ocean heat uptake as a major source of spread  
387    in transient climate change simulations. *Geophys. Res. Lett.*, **36**, L22701,  
388    doi:10.1029/2009GL040845.
- 389    Delworth, T. L., and Coauthors, 2012: Simulated Climate and Climate Change in the  
390    GFDL CM2.5 High-Resolution Coupled Climate Model. *J. Clim.*, **25**, 2755–2781,  
391    doi:10.1175/JCLI-D-11-00316.1.
- 392    Downes, S. M., and Coauthors, 2015: An assessment of Southern Ocean water masses  
393    and sea ice during 1988–2007 in a suite of interannual CORE-II simulations.  
394    *Ocean Model.*, **94**, 67–94, doi:10.1016/j.ocemod.2015.07.022.
- 395    Exarchou, E., T. Kuhlbrodt, J. M. Gregory, and R. S. Smith, 2014: Ocean Heat Uptake  
396    Processes: A Model Intercomparison. *J. Clim.*, **28**, 887–908, doi:10.1175/JCLI-  
397    D-14-00235.1.
- 398    Farneti, R., and Coauthors, 2015: An assessment of Antarctic Circumpolar Current  
399    and Southern Ocean meridional overturning circulation during 1958–2007 in  
400    a suite of interannual CORE-II simulations. *Ocean Model.*, **93**, 84–120,  
401    doi:10.1016/j.ocemod.2015.07.009.
- 402    Frierson, D. M. W., and Coauthors, 2013: Contribution of ocean overturning  
403    circulation to tropical rainfall peak in the Northern Hemisphere. *Nat. Geosci.*,  
404    **6**, 940–944.
- 405    Frölicher, T. L., J. L. Sarmiento, D. J. Paynter, J. P. Dunne, J. P. Krasting, and M. Winton,  
406    2014: Dominance of the Southern Ocean in Anthropogenic Carbon and Heat  
407    Uptake in CMIP5 Models. *J. Clim.*, **28**, 862–886, doi:10.1175/JCLI-D-14-  
408    00117.1.
- 409    Geoffroy, O., D. Saint-Martin, G. Bellon, A. Volodire, D. J. L. Olivié, and S. Tytéca, 2013:  
410    Transient Climate Response in a Two-Layer Energy-Balance Model. Part II:  
411    Representation of the Efficacy of Deep-Ocean Heat Uptake and Validation for  
412    CMIP5 AOGCMs. *J. Clim.*, **26**, 1859–1876, doi:10.1175/JCLI-D-12-00196.1.
- 413    Gregory, J. M., and J. F. B. Mitchell, 1997: The climate response to CO<sub>2</sub> of the Hadley  
414    Centre coupled AOGCM with and without flux adjustment. *Geophys. Res. Lett.*,  
415    **24**, 1943–1946, doi:10.1029/97GL01930.
- 416    ——, and Coauthors, 2004: A new method for diagnosing radiative forcing and  
417    climate sensitivity. *Geophys. Res. Lett.*, **31**, L03205,  
418    doi:10.1029/2003GL018747.

- 419 ——, and Coauthors, 2005: A model intercomparison of changes in the Atlantic  
420 thermohaline circulation in response to increasing atmospheric CO<sub>2</sub>  
421 concentration. *Geophys. Res. Lett.*, **32**, L12703, doi:10.1029/2005GL023209.
- 422 ——, T. Andrews, and P. Good, 2015: The inconstancy of the transient climate  
423 response parameter under increasing CO<sub>2</sub>. *Philos. Trans. R. Soc. Lond. Math.*  
424 *Phys. Eng. Sci.*, **373**, doi:10.1098/rsta.2014.0417.  
425 <http://rsta.royalsocietypublishing.org/content/373/2054/20140417.abstract>  
426
- 427 Gregory, M. J., 2000: Vertical heat transports in the ocean and their effect on time-  
428 dependent climate change. *Clim. Dyn.*, **16**, 501–515,  
429 doi:10.1007/s003820000059.
- 430 Gupta, A. S., L. C. Muir, J. N. Brown, S. J. Phipps, P. J. Durack, D. Monselesan, and S. E.  
431 Wijffels, 2012: Climate Drift in the CMIP3 Models. *J. Clim.*, **25**, 4621–4640,  
432 doi:10.1175/JCLI-D-11-00312.1.
- 433 Hansen, J., A. Lacis, D. Rind, G. Russell, P. Stone, I. Fung, R. Ruedy, and J. Lerner, 1984:  
434 Climate Sensitivity: Analysis of Feedback Mechanisms. *Climate Processes and*  
435 *Climate Sensitivity*, American Geophysical Union, 130–163  
436 <http://dx.doi.org/10.1029/GM029p0130>.
- 437 Hasselmann, K., R. Sausen, E. Maier-Reimer, and R. Voss, 1993: On the cold start  
438 problem in transient simulations with coupled atmosphere-ocean models.  
439 *Clim. Dyn.*, **9**, 53–61, doi:10.1007/BF00210008.
- 440 Kang, S. M., and S.-P. Xie, 2014: Dependence of Climate Response on Meridional  
441 Structure of External Thermal Forcing. *J. Clim.*, **27**, 5593–5600,  
442 doi:10.1175/JCLI-D-13-00622.1.
- 443 Kostov, Y., K. C. Armour, and J. Marshall, 2014: Impact of the Atlantic meridional  
444 overturning circulation on ocean heat storage and transient climate change.  
445 *Geophys. Res. Lett.*, **41**, 2108–2116, doi:10.1002/2013GL058998.
- 446 de Lavergne, C., J. B. Palter, E. D. Galbraith, R. Bernardello, and I. Marinov, 2014:  
447 Cessation of deep convection in the open Southern Ocean under  
448 anthropogenic climate change. *Nat. Clim Change*, **4**, 278–282.
- 449 Liang, M.-C., L.-C. Lin, K.-K. Tung, Y. L. Yung, and S. Sun, 2013a: Transient Climate  
450 Response in Coupled Atmospheric–Ocean General Circulation Models. *J.*  
451 *Atmospheric Sci.*, **70**, 1291–1296, doi:10.1175/JAS-D-12-0338.1.
- 452 ——, ——, ——, ——, and ——, 2013b: Impact of Climate Drift on Twenty-First-  
453 Century Projection in a Coupled Atmospheric–Ocean General Circulation  
454 Model. *J. Atmospheric Sci.*, **70**, 3321–3327, doi:10.1175/JAS-D-13-0149.1.

- 455 Medhaug, I., and T. Furevik, 2011: North Atlantic 20th century multidecadal  
456 variability in coupled climate models: sea surface temperature and ocean  
457 overturning circulation. *Ocean Sci.*, **7**, 389–404, doi:10.5194/os-7-389-2011.
- 458 Meehl, G. A., W. M. Washington, W. D. Collins, J. M. Arblaster, A. Hu, L. E. Buja, W. G.  
459 Strand, and H. Teng, 2005: How Much More Global Warming and Sea Level  
460 Rise? *Science*, **307**, 1769–1772, doi:10.1126/science.1106663.
- 461 Meredith, M. P., A. C. Naveira Garabato, A. M. Hogg, and R. Farneti, 2012: Sensitivity  
462 of the Overturning Circulation in the Southern Ocean to Decadal Changes in  
463 Wind Forcing. *J. Clim.*, **25**, 99–110, doi:10.1175/2011JCLI4204.1.
- 464 Morrison, A. K., and A. M. Hogg, 2013: On the Relationship between Southern Ocean  
465 Overturning and ACC Transport. *J. Phys. Oceanogr.*, **43**, 140–148,  
466 doi:10.1175/JPO-D-12-057.1.
- 467 Newsom, E. R., C. M. Bitz, F. O. Bryan, R. Abernathay, and P. R. Gent, 2016: Southern  
468 Ocean Deep Circulation and Heat Uptake in a High-Resolution Climate Model.  
469 *J. Clim.*, **29**, 2597–2619, doi:10.1175/JCLI-D-15-0513.1.
- 470 Orsi, A., G. Johnson, and J. Bullister, 1999: Circulation, mixing, and production of  
471 Antarctic Bottom Water. *Prog. Oceanogr.*, **43**, 55–109.
- 472 Purkey, S. G., and G. C. Johnson, 2010: Warming of Global Abyssal and Deep Southern  
473 Ocean Waters between the 1990s and 2000s: Contributions to Global Heat  
474 and Sea Level Rise Budgets. *J. Clim.*, **23**, 6336–6351,  
475 doi:10.1175/2010JCLI3682.1.
- 476 ——, and ——, 2012: Global Contraction of Antarctic Bottom Water between the  
477 1980s and 2000s. *J. Clim.*, **25**, 5830–5844, doi:10.1175/JCLI-D-11-00612.1.
- 478 ——, and ——, 2013: Antarctic Bottom Water Warming and Freshening:  
479 Contributions to Sea Level Rise, Ocean Freshwater Budgets, and Global Heat  
480 Gain. *J. Clim.*, **26**, 6105–6122, doi:10.1175/JCLI-D-12-00834.1.
- 481 Raper, S. C. B., J. M. Gregory, and R. J. Stouffer, 2002: The Role of Climate Sensitivity  
482 and Ocean Heat Uptake on AOGCM Transient Temperature Response. *J. Clim.*,  
483 **15**, 124–130, doi:10.1175/1520-0442(2002)015<0124:TROCSA>2.0.CO;2.
- 484 Rose, B. E. J., K. C. Armour, D. S. Battisti, N. Feldl, and D. D. B. Koll, 2014: The  
485 dependence of transient climate sensitivity and radiative feedbacks on the  
486 spatial pattern of ocean heat uptake. *Geophys. Res. Lett.*, **41**, 1071–1078,  
487 doi:10.1002/2013GL058955.
- 488 Rugenstein, M. A. A., M. Winton, R. J. Stouffer, S. M. Griffies, and R. Hallberg, 2013:  
489 Northern High-Latitude Heat Budget Decomposition and Transient Warming.  
490 *J. Clim.*, **26**, 609–621, doi:10.1175/JCLI-D-11-00695.1.

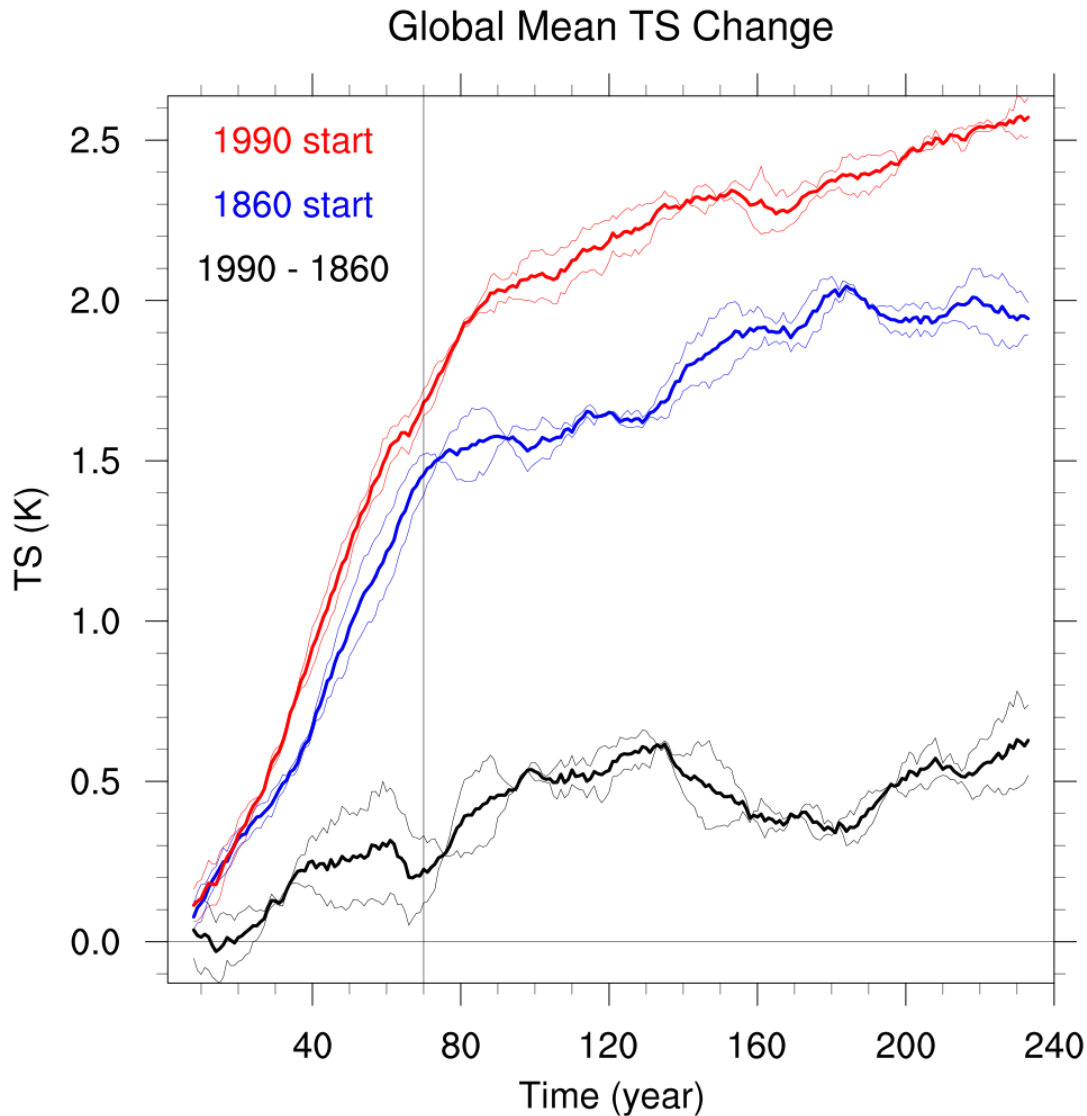
- 491 ——, K. Caldeira, and R. Knutti, 2016a: Dependence of global radiative feedbacks on  
492 evolving patterns of surface heat fluxes. *Geophys. Res. Lett.*, 2016GL070907,  
493 doi:10.1002/2016GL070907.
- 494 ——, J. Sedláček, and R. Knutti, 2016b: Nonlinearities in patterns of long-term ocean  
495 warming. *Geophys. Res. Lett.*, **43**, 3380–3388, doi:10.1002/2016GL068041.
- 496 Russell, J. L., R. J. Stouffer, and K. W. Dixon, 2006: Intercomparison of the Southern  
497 Ocean Circulations in IPCC Coupled Model Control Simulations. *J. Clim.*, **19**,  
498 4560–4575, doi:10.1175/JCLI3869.1.
- 499 Soden, B. J., I. M. Held, R. Colman, K. M. Shell, J. T. Kiehl, and C. A. Shields, 2008:  
500 Quantifying Climate Feedbacks Using Radiative Kernels. *J. Clim.*, **21**, 3504–  
501 3520, doi:10.1175/2007JCLI2110.1.
- 502 Solomon, S., 2007: *Climate change 2007—the physical science basis: Working group I  
503 contribution to the fourth assessment report of the IPCC*. Cambridge University  
504 Press.,
- 505 Stocker, T. F., and Coauthors, 2013: Climate Change 2013 The Physical Science Basis.
- 506 Stouffer, R. J., and Coauthors, 2006a: GFDL’s CM2 Global Coupled Climate Models.  
507 Part IV: Idealized Climate Response. *J. Clim.*, **19**, 723–740,  
508 doi:10.1175/JCLI3632.1.
- 509 Stouffer, R. J., J. Russell, and M. J. Spelman, 2006b: Importance of oceanic heat uptake  
510 in transient climate change. *Geophys. Res. Lett.*, **33**, L17704,  
511 doi:10.1029/2006GL027242.
- 512 Taylor, K. E., R. J. Stouffer, and G. A. Meehl, 2012: An overview of CMIP5 and the  
513 experiment design. *Bull. Am. Meteorol. Soc.*, **93**, 485–498, doi:10.1175/BAMS-  
514 D-11-00094.1.
- 515 Trossman, D. S., J. B. Palter, T. M. Merlis, Y. Huang, and Y. Xia, 2016: Large-scale  
516 ocean circulation-cloud interactions reduce the pace of transient climate  
517 change. *Geophys. Res. Lett.*, **43**, 2016GL067931, doi:10.1002/2016GL067931.
- 518 Vecchi, G. A., and Coauthors, 2014: On the seasonal forecasting of regional tropical  
519 cyclone activity. *J. Clim.*, **27**, 7994–8016, doi:10.1175/JCLI-D-14-00158.1.
- 520 Weaver, A. J., M. Eby, M. Kienast, and O. A. Saenko, 2007: Response of the Atlantic  
521 meridional overturning circulation to increasing atmospheric CO<sub>2</sub>:  
522 Sensitivity to mean climate state. *Geophys. Res. Lett.*, **34**, L05708,  
523 doi:10.1029/2006GL028756.
- 524 Winton, M., 2003: On the Climatic Impact of Ocean Circulation. *J. Clim.*, **16**, 2875–  
525 2889, doi:10.1175/1520-0442(2003)016<2875:OTCIOO>2.0.CO;2.

- 526 ——, K. Takahashi, and I. M. Held, 2010: Importance of Ocean Heat Uptake Efficacy  
527 to Transient Climate Change. *J. Clim.*, **23**, 2333–2344,  
528 doi:10.1175/2009JCLI3139.1.
- 529 ——, S. M. Griffies, B. L. Samuels, J. L. Sarmiento, and T. L. Frölicher, 2013:  
530 Connecting Changing Ocean Circulation with Changing Climate. *J. Clim.*, **26**,  
531 2268–2278, doi:10.1175/JCLI-D-12-00296.1.
- 532 ——, W. G. Anderson, T. L. Delworth, S. M. Griffies, W. J. Hurlin, and A. Rosati, 2014:  
533 Has coarse ocean resolution biased simulations of transient climate  
534 sensitivity? *Geophys. Res. Lett.*, **41**, 2014GL061523,  
535 doi:10.1002/2014GL061523.
- 536 Xie, P., and G. K. Vallis, 2012: The passive and active nature of ocean heat uptake in  
537 idealized climate change experiments. *Clim. Dyn.*, **38**, 667–684,  
538 doi:10.1007/s00382-011-1063-8.
- 539 Zhang, R., S. M. Kang, and I. M. Held, 2010: Sensitivity of Climate Change Induced by  
540 the Weakening of the Atlantic Meridional Overturning Circulation to Cloud  
541 Feedback. *J. Clim.*, **23**, 378–389, doi:10.1175/2009JCLI3118.1.
- 542 Zhang, S., M. J. Harrison, A. Rosati, and A. Wittenberg, 2007: System Design and  
543 Evaluation of Coupled Ensemble Data Assimilation for Global Oceanic Climate  
544 Studies. *Mon. Weather Rev.*, **135**, 3541–3564, doi:10.1175/MWR3466.1.

545

Feedback (W/m <sup>2</sup> /K)	T+WV	Albedo	Cloud	Total
1990 start	-2.00	0.28	0.61 (0.52)	-1.12 (-1.21)
1860 start	-2.00	0.23	0.51 (0.28)	-1.27 (-1.50)
1990 - 1860	-0.00	0.05	0.10 (0.24)	0.15 (0.29)

547 Table 1. Transient radiative feedbacks during the CO<sub>2</sub> stabilization period calculated  
 548 using radiative kernels. Corrected total feedback using the average TOA radiation and  
 549 surface temperature change during the CO<sub>2</sub> stabilization period and corrected cloud  
 550 feedback using the corrected total feedback while assuming the accuracy of kernel-based  
 551 temperature, water vapor and albedo feedbacks are shown in the parentheses.

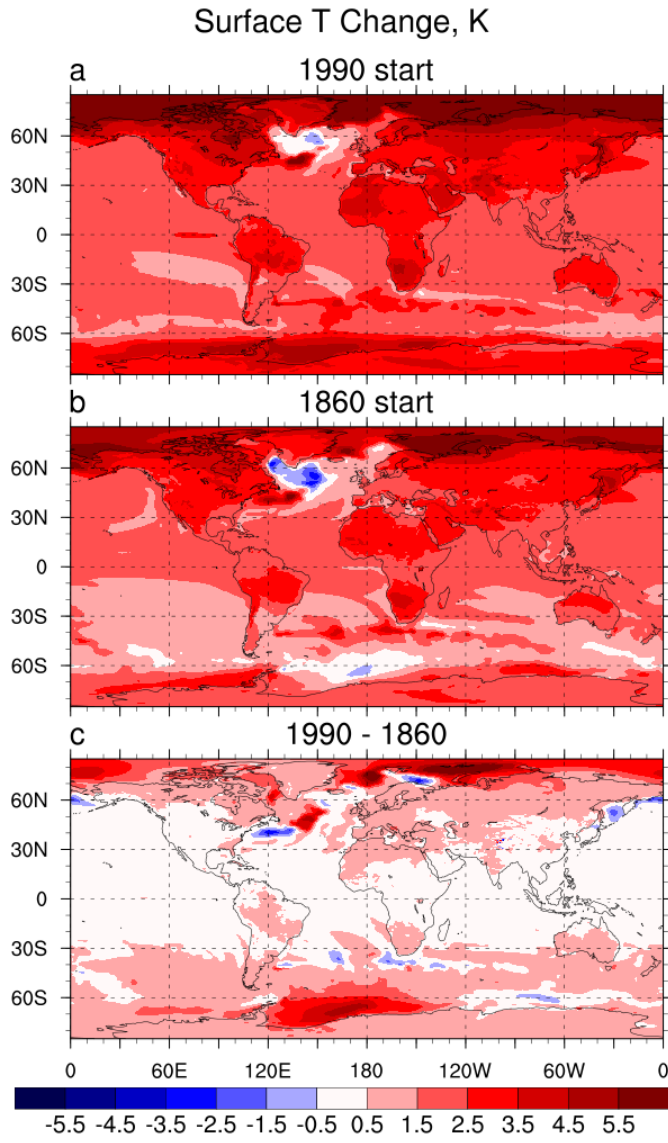


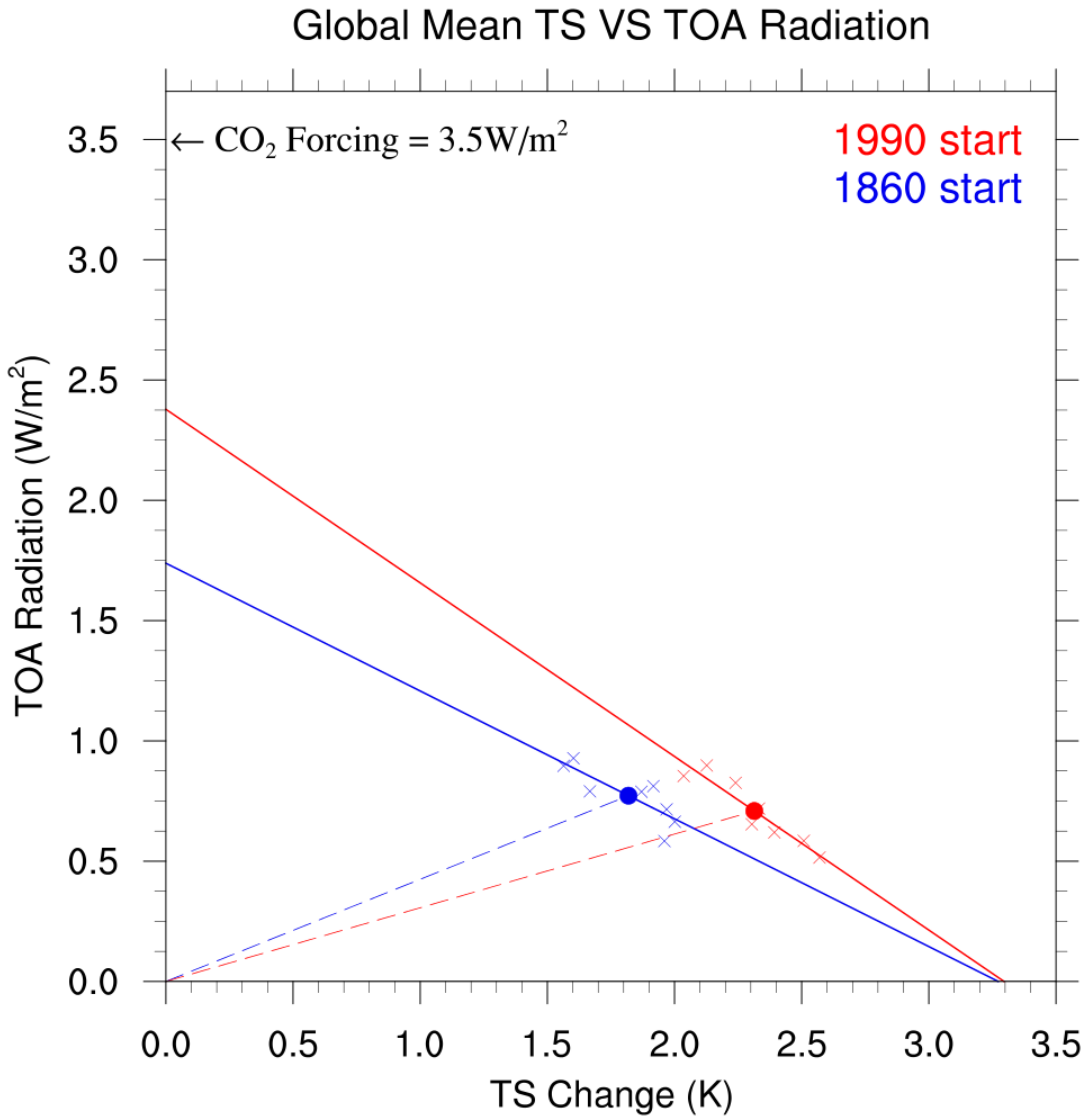
552

553 Figure 1. Global mean surface temperature change from the 1990-start (red) and 1860-  
 554 start (blue) runs. Black lines show the difference between 1990-start and 1860-start runs.  
 555 Thin lines are from the individual ensembles, whereas thick lines are the two-ensemble  
 556 mean. Data are plotted as 15-year running mean. The thin vertical line indicates the time  
 557 of CO<sub>2</sub> doubling, after which CO<sub>2</sub> is held fixed.

558

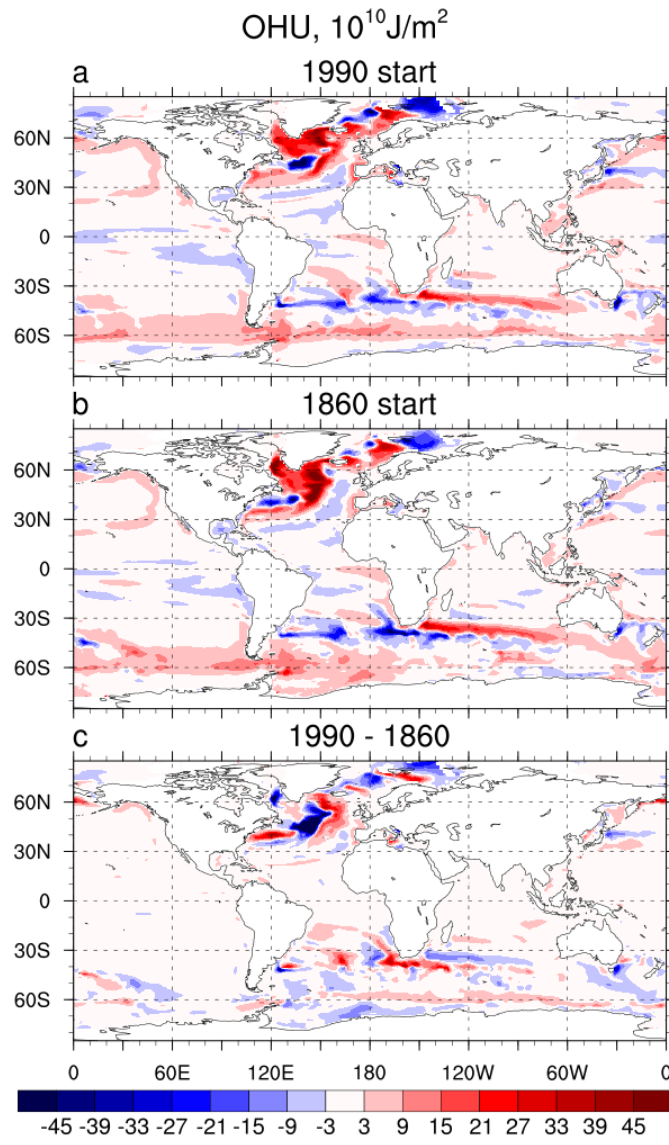
559     Figure 2. Ensemble mean surface temperature change from the 1990-start run (a), the  
560     1860-start run (b) and the difference between the two. Changes are averaged over the last  
561     50 years of the simulations.





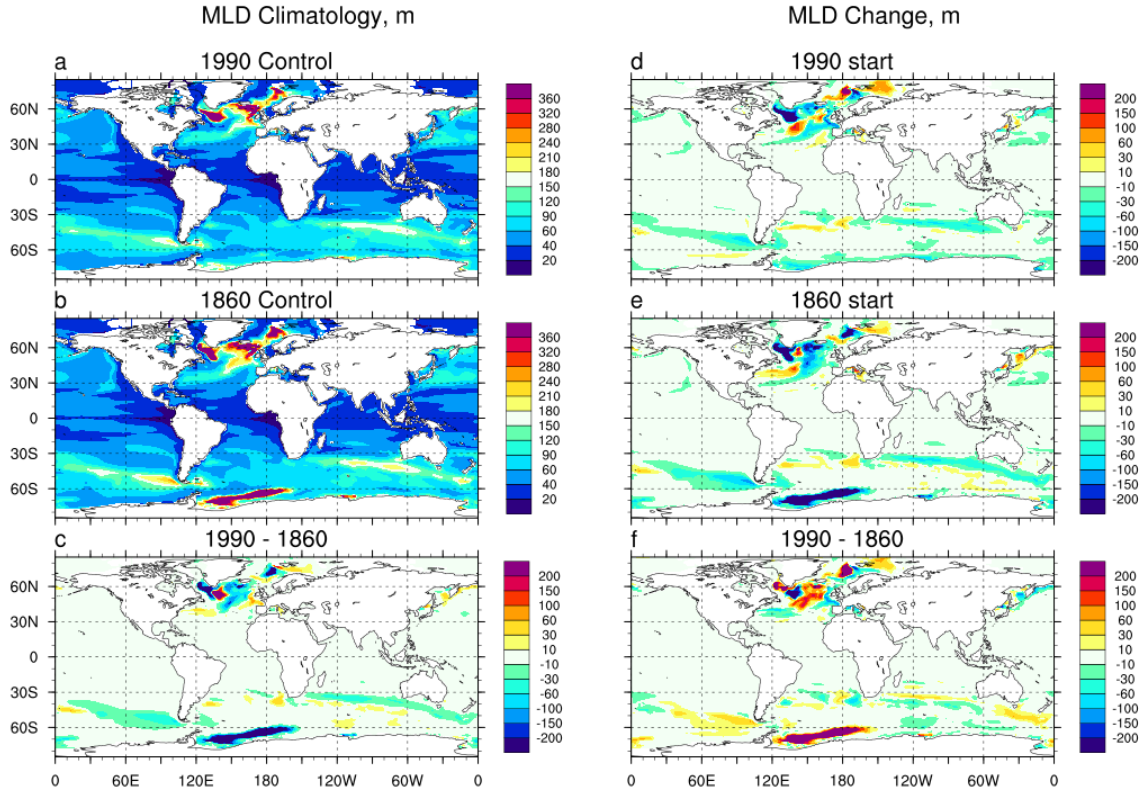
562

563 Figure 3. Scatter plot of global mean TOA radiation and surface temperature change  
 564 using 20 year averages during the CO<sub>2</sub> stabilization period (crosses). The round dots  
 565 show averages of the entire stabilization period. The solid lines fit the crosses, whereas  
 566 the dashed lines connect the round dots and the (0,0) point. The global mean CO<sub>2</sub>  
 567 radiative forcing is pointed out on the y-axis. All data are shown as the two ensemble  
 568 mean.



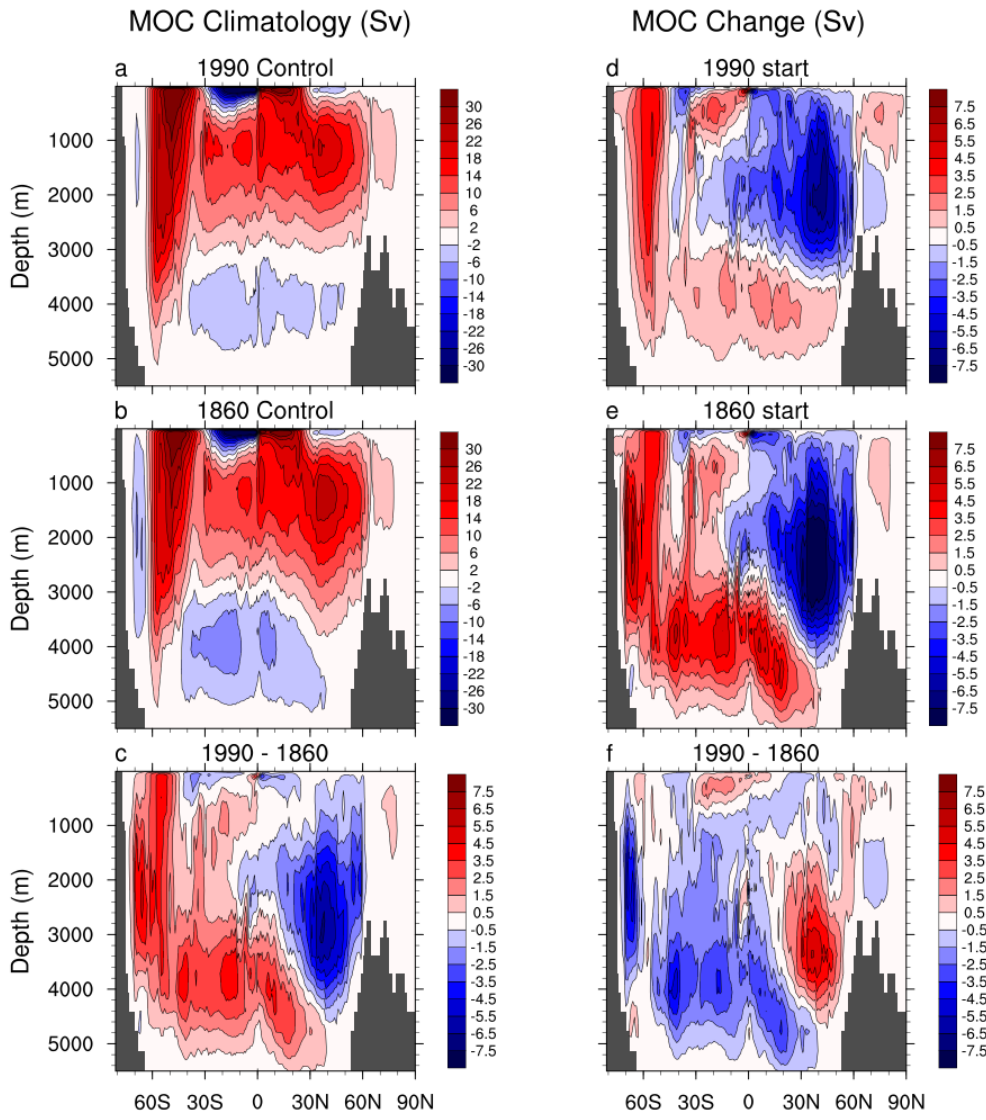
569

570 Figure 4. Ensemble mean surface ocean heat uptake calculated as changes in surface heat  
 571 flux integrated over the entire 240 years of the simulation. Positive values indicate  
 572 downward heat fluxes. (a) and (b) are results from the 1990-start and 1860-start runs,  
 573 respectively. (c) is the difference between the two. Zonal integrals of the heat uptake for  
 574 the high-latitudes and the tropics are provided in Figure 8.



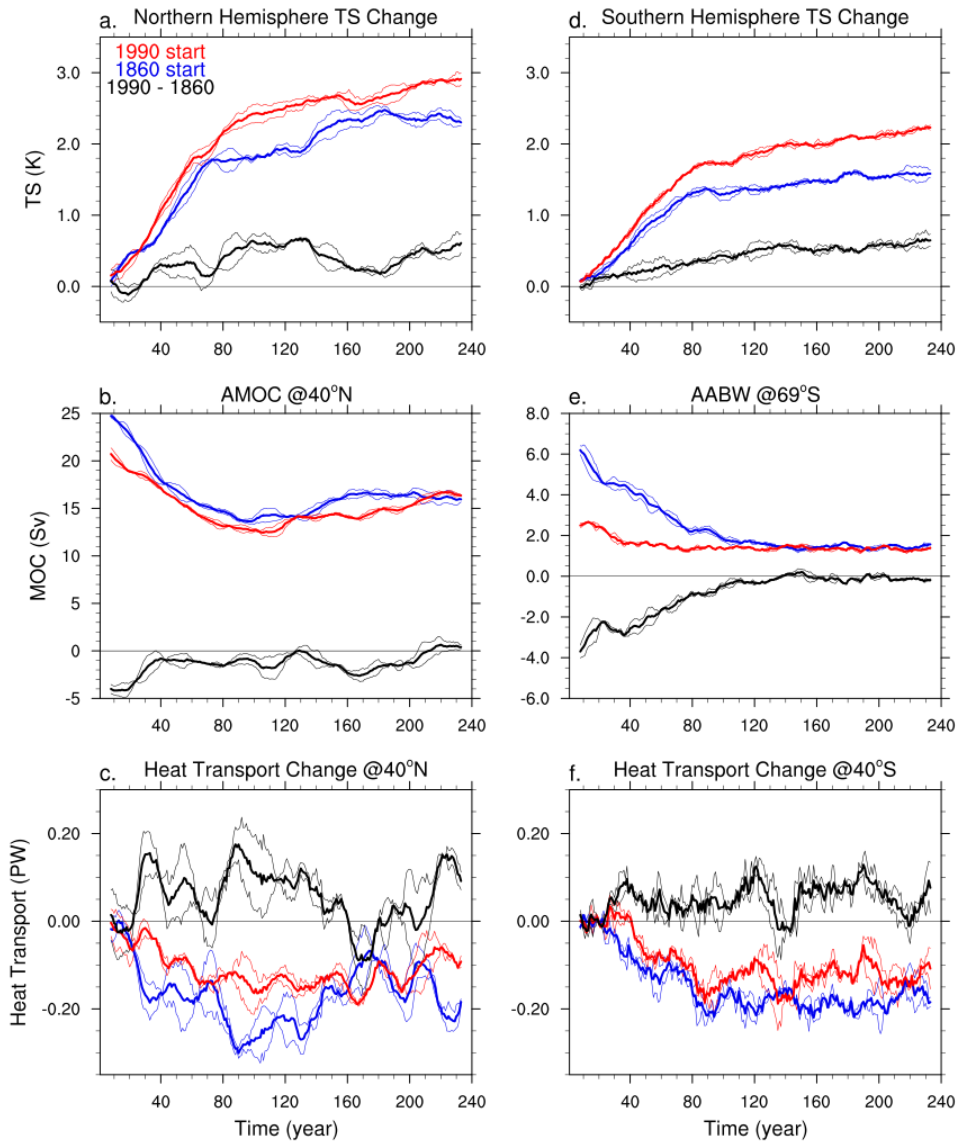
575

576 Figure 5. Ensemble mean mixed-layer depth climatology (a-c) and change (d-f).  
 577 Climatology is calculated as the 240-year average from the control runs, whereas change  
 578 is calculated as the average over the last 50 years of the perturbed runs. Top and middle  
 579 rows are results from the 1990-start and 1860-start runs, respectively. The bottom row is  
 580 the difference between the two.



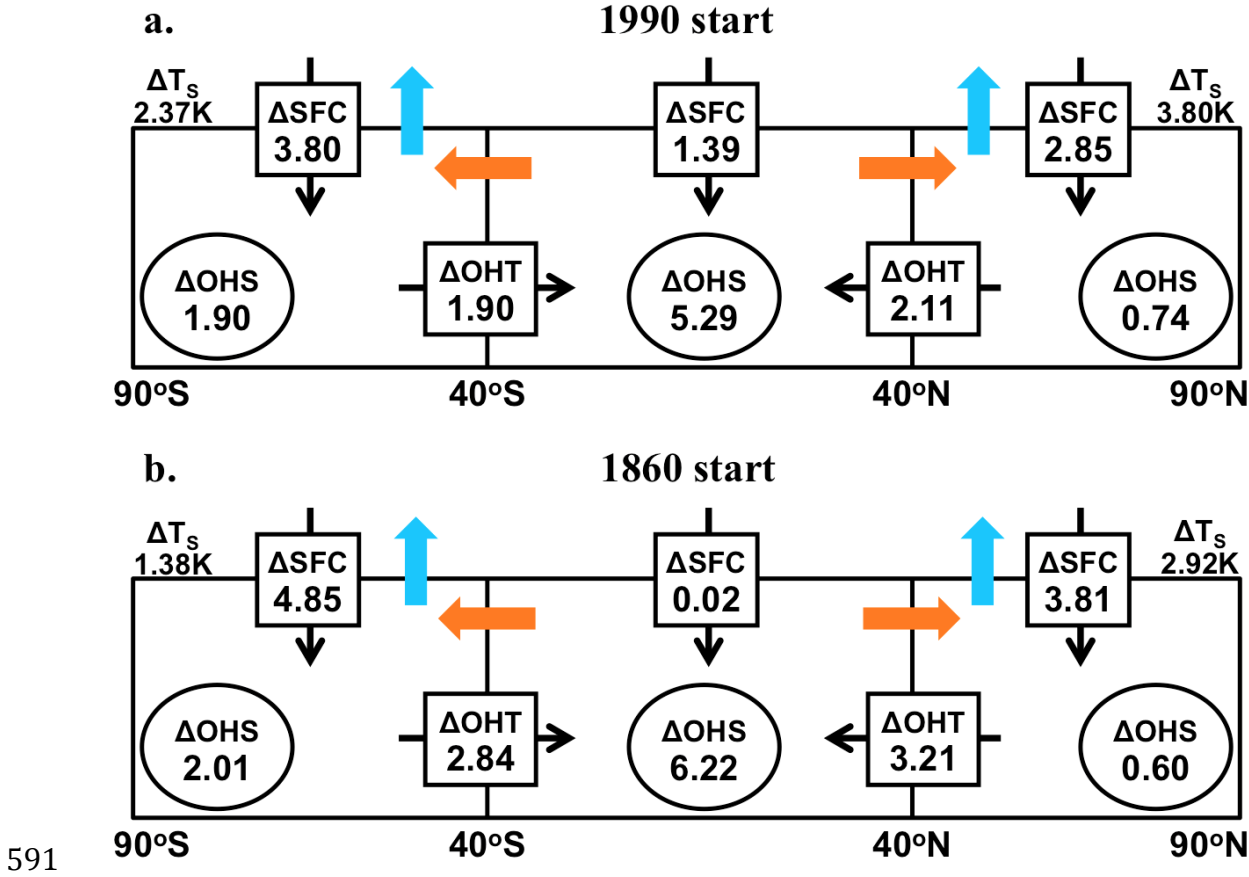
581

582 Figure 6. Same as Fig. 5 except for the zonally integrated stream function.



583

584 Figure 7. Time series of hemispheric surface warming (a and d), AMOC (b), AABW (e)  
 585 and changes in the zonally integrated poleward global ocean heat transport (c and f).  
 586 AMOC and AABW are calculated at 40°N and 69°S, respectively, and their control run  
 587 anomalies are removed to reduce the impact of model drift. Ocean heat transport is  
 588 calculated indirectly as the difference between ocean heat storage tendency and changes  
 589 in surface heat flux. Thin lines are from the individual ensembles, whereas thick lines are  
 590 the two ensemble mean. Data are plotted as 15-year running mean.



592 Figure 8. Ensemble mean changes in surface heat flux (SFC), changes in meridional  
 593 ocean heat transport (OHT) and ocean heat storage tendency (OHS) averaged over the  
 594 entire simulation. Variables are integrated over three climate zones, which are bounded  
 595 by the  $40^\circ$  latitude, and divided by the global earth surface area. Unit is  $0.1\text{W/m}^2$ .  $\Delta OHT$   
 596 is calculated as the difference between  $\Delta OHS$  and  $\Delta SFC$  in the high-latitude zones. Black  
 597 arrows indicate the direction of the heat flux changes. Surface temperature changes  
 598 poleward of  $40^\circ$  averaged over the last 50 years of the simulations are also shown. Blue  
 599 and orange arrows indicate the direction of the climatological SFC and OHT,  
 600 respectively.

Figure 1. Global mean surface temperature change from the 1990-start (red) and 1860-start (blue) runs. Black lines show the difference between 1990-start and 1860-start runs. Thin lines are from the individual ensembles, whereas thick lines are the two-ensemble mean. Data are plotted as 15-year running mean. The thin vertical line indicates the time of CO<sub>2</sub> doubling, after which CO<sub>2</sub> is held fixed.

Figure 2. Ensemble mean surface temperature change from the 1990-start run (a), the 1860-start run (b) and the difference between the two. Changes are averaged over the last 50 years of the simulations.

Figure 3. Scatter plot of global mean TOA radiation and surface temperature change using 20 year averages during the CO<sub>2</sub> stabilization period (crosses). The round dots show averages of the entire stabilization period. The solid lines fit the crosses, whereas the dashed lines connect the round dots and the (0,0) point. The global mean CO<sub>2</sub> radiative forcing is pointed out on the y-axis. All data are shown as the two ensemble mean.

Figure 4. Ensemble mean surface ocean heat uptake calculated as changes in surface heat flux integrated over the entire 240 years of the simulation. Positive values indicate downward heat fluxes. (a) and (b) are results from the 1990-start and 1860-start runs, respectively. (c) is the difference between the two. Zonal integrals of the heat uptake for the high-latitudes and the tropics are provided in Figure 8.

Figure 5. Ensemble mean mixed-layer depth climatology (a-c) and change (d-f). Climatology is calculated as the 240-year average from the control runs, whereas change is calculated as the average over the last 50 years of the perturbed runs. Top and middle rows are results from the 1990-start and 1860-start runs, respectively. The bottom row is the difference between the two.

Figure 6. Same as Fig. 5 except for the zonally integrated stream function.

Figure 7. Time series of hemispheric surface warming (a and d), AMOC (b), AABW (e) and changes in the zonally integrated poleward global ocean heat transport (c and f). AMOC and AABW are calculated at 40°N and 69°S, respectively, and their control run anomalies are removed to reduce the impact of model drift. Ocean heat transport is calculated indirectly as the difference between ocean heat storage tendency and changes in surface heat flux. Thin lines are from the individual ensembles, whereas thick lines are the two ensemble mean. Data are plotted as 15-year running mean.

Figure 8. Ensemble mean changes in surface heat flux (SFC), changes in meridional ocean heat transport (OHT) and ocean heat storage tendency (OHS) averaged over the entire simulation. Variables are integrated over three climate zones, which are bounded by the 40° latitude, and divided by the global earth surface area. Unit is 0.1W/m<sup>2</sup>.  $\Delta$ OHT is calculated as the difference between  $\Delta$ OHS and  $\Delta$ SFC in the high-latitude zones. Black arrows indicate the direction of the heat flux changes. Surface temperature changes poleward of 40° averaged over the last 50 years of the simulations are also shown. Blue

and orange arrows indicate the direction of the climatological SFC and OHT, respectively.